Journal of Materials Chemistry A

ROYAL SOCIETY OF CHEMISTRY

PAPER

View Article Online
View Journal | View Issue

Open Access Article. Published on 28 January 2026. Downloaded on 6/13/2026 11:29:15 AM.
This article is licensed under a Creative Commons Attribution-NonCommercial 3.0 Unported Licence.

Check for updates

Cite this: J. Mater. Chem. A, 2026, 14, 10882

Aluminium siting in zeolite RTH from a combined machine learning – NMR approach

Daniel Willimetz, †[a] Joaquin Martínez-Ortigosa, †[bc] Deborah Brako-Amoafo, [ad] Lukáš Grajciar, [a] J. Alejandro Vidal-Moya, [b] Carlos Bornes, [a] Vincent Sarou-Kanian, [e] Fernando Rey, [b] Teresa Blasco *[b] and Christopher J. Heard *[a]

Received 13th November 2025
Accepted 27th January 2026

DOI: 10.1039/d5ta09253a

rsc.li/materials-a

Determining the distribution of aluminium in zeolite frameworks remains a significant challenge, due to the limited sensitivity of conventional characterization techniques. To overcome this issue, we have developed a procedure which combines experimental two-dimensional (2D) solid-state NMR spectroscopy with machine learning (ML) techniques. To validate the approach, we have applied it to achieve a detailed assignment of Al environments in zeolite RTH. A reactive ML potential was used to model long-timescale framework dynamics under realistic conditions, including temperature and hydration, alongside the accurate prediction of isotropic NMR chemical shifts. Comparison between theoretical and experimental spectra reveals that Al preferentially occupies the T_2 sites, with under-population of the other T-sites. The excellent agreement between computed and observed NMR data demonstrates that this ML-augmented spectroscopic approach is a powerful tool for quantitative elucidation of Al distributions in structurally complex zeolites, going far beyond the limitations of traditional quantum chemical approaches.

1. Introduction

The framework structure and composition of zeolites, in particular the distribution of aluminium atoms, significantly influence their acidity, stability, and catalytic performance.[1–7] For example, it has been shown that controlling the balance of Al siting between intersection and channel sites has a profound effect on catalytic selectivity, activity and longevity in hydrocarbon transformations over zeolite ZSM-5 (ref. 3, 4, 6 and 8) and zeolite ITR,[9] supported also by theoretical calculations.[10] Furthermore, the extent of Al pairing, in which the proximity of other Al atoms influences the character of a given Al centre, has been shown to impact on catalytic activity. For example, Tabor *et al.* attributed a 5–8 times increase in propene to olefins conversion rate to the presence of proximate Brønsted sites, caused by Al pairing in ZSM-5.[11]

It is therefore a long term aim in zeolite science to control the location of aluminium atoms in the framework, in order to achieve bottom-up design of optimised catalysts.[12,13] As a result, intensive research activity has been undertaken to elucidate how aluminium positioning in the framework is influenced by various synthesis parameters, including the balance of organic structure directing agents (OSDAs),[14] mixtures of OSDA with inorganic structure directing agents,[15] the type of mineralizing agents (fluoride or hydroxide)[1] or the presence of pore-filling agents.[16] For a comprehensive perspective on these factors, we direct the reader to ref. 17.

In addition to the challenges in controlling aluminium location, there are significant difficulties in characterising the aluminium siting, which is not amenable either to standard techniques that provide averaged data, such as X-ray diffraction, or to imaging methods such as electron microscopy, due to issues of resolution and beam-damage. Common approaches to determine aluminium positioning include the indirect observation of Al positions by measuring the location and interactions of extra-framework counter-ions and probe molecules. However, it has recently been shown that the interpretation of Al positioning *via* probe molecules is challenging, and the complex chemical environment inside the zeolite pore, involving for example, probe–probe interactions and protonation may lead to incorrect assignments.[18] Another approach employs direct observation of framework Al atoms, using methods such as anomalous X-ray diffraction,[19–21] which promises to identify the occupation of both isolated and paired

[a]Department of Physical and Macromolecular Chemistry, Charles University in Prague, Hlavova 8, 12800, Praha 2, Czech Republic. E-mail: heardc@natur.cuni.cz

[b]Instituto de Tecnología Química, Universitat Politècnica de València – Consejo Superior de Investigaciones Científicas (UPV-CSIC), Avenida Los Naranjos s/n, 46022 Valencia, Spain. E-mail: tblasco@itq.upv.es

[c]Laboratorio de Nanotecnología Molecular, Departamento de Química Inorgánica, Universidad de Alicante, Ctra. San Vicente-Alicante s/n, 03690, Alicante, Spain

[d]EaStChem School of Chemistry, University of St Andrews, Purdie Building, St Andrews KY16 9ST, UK

[e]CEMHTI-CNRS, CNRS UPR3079, 1d Avenue de la Recherche Scientifique, 45071 Orléans Cedex 2, France

† These authors contributed equally.

This journal is © The Royal Society of Chemistry 2026

Open Access Article. Published on 28 January 2026. Downloaded on 6/13/2026 11:29:15 AM. This article is licensed under a Creative Commons Attribution-NonCommercial 3.0 Unported Licence.

Al atoms, but suffers from high complexity of analysis, and is currently possible only with highly specialised experimental equipment.

By contrast, solid-state NMR spectroscopy offers unique advantages as it is a readily available technique, which can probe aluminium environments both indirectly and directly, and enables correlation experiments that provide complementary structural information. *Operando* ss-NMR is increasingly commonplace, and can provide insight into dynamic events within the pore, such as the progress of adsorption or reaction processes as a function of temperature or reactant mixture. Solid-state NMR spectroscopy, particularly ^{27}Al and ^{29}Si NMR, is therefore a powerful tool for probing the local structure of zeolites and the role of environmental variables.[1,22–28] In non-defective siliceous zeolites ^{29}Si NMR can be used to quantify the amount of each T-site, as ^{29}Si peaks of Q^4(0Al) species are often sharp.[29,30] However, the addition of Al to zeolites leads to a broadening of the ^{29}Si resonances which hinders the identification of T-sites.[31]

One of the more common approaches to determine the distribution of aluminium among multiple T-sites in zeolite frameworks has been the analysis of ^{27}Al multiple-quantum magic angle spinning (MQMAS) NMR spectra.[24,32] The increased resolution achieved in MQMAS allows identification of various tetrahedral Al sites when combined with computational calculations of aluminium at specific T-sites. Unfortunately, the increased resolution of ^{27}Al MQMAS in zeolites is often insufficient to unambiguously assign T-sites. However, previous studies have overcome this limitation by employing recoupling methods that probe ^{29}Si–^{27}Al connectivity, thereby facilitating Al siting determination.[22,33,34] Regardless of the specific NMR approach employed, accurate assignment of experimental spectra to specific T-sites typically requires comparison with calculated NMR parameters.

With few recent exceptions, the contribution of computational methods to the assignment of NMR spectra has been limited to the calculation of chemical shifts, based on small numbers of static snapshots of simplified structural models. Often, such calculations are performed in the athermal regime using electronic structure methods, such as density functional theory.[22,23] However, it has been shown recently that significant differences may be observed between 0 K local minima and properly thermalized zeolite structures, and even at room temperature, temperature effects manifest themselves through dynamical averaging of a broad range of configurations, leading to changes in chemical shift.[35,36] In addition, explicit molecules contained within the pore voids of the zeolite, which are usually discounted in modelling, has been seen to affect framework acidity and charge distributions, and thus the NMR spectrum.[35,36] In summary, even under mild conditions, there is a need to move towards *operando* modelling in zeolites, in order to close the gap between experiment and theory.

The recent advent of machine learning methods, in particular neural network-based machine learning interatomic potentials (MLIP), has opened the possibility to gather structural information from long, nanosecond-timescale dynamical simulations, using large, flexible zeolite models, from which averaged data can be extracted under conditions which more closely reproduce experiment.[37–39] It has been shown in several recent works, that even at room temperature, where drastic changes to zeolite structure are not expected, that NMR signals are significantly affected – necessitating dynamical simulations that go beyond the timescales available to density functional theory.[35,36] Such long simulations have been utilized, for example, to predict the instability of zeolite frameworks, model structural transitions, such as melting and recrystallization, and even the mobility of encapsulated metal particles through the zeolite pore system.[38–42] In addition to extending the timescale of simulations, the structure–spectra relationship has been explored computationally in several recent ML-driven works, primarily using linear regression methods. These include the Least Absolute Shrinkage and Selection Operator (LASSO) approach, which benefits from interpretability, but suffers from typically low dimensionality and a constraint of linearity, as well as the need for user-chosen features which may miss important variables,[35,43] and Kernel Ridge Regression (KRR), which have shown superior performance,[36] but lack for physical interpretability, to predict chemical shifts and more recently, chemical shielding tensors[44] and electric field gradient (EFG) tensors.[43,45,46] Such methods have shown promise for several zeolite-relevant nuclei, including ^{27}Al, ^{29}Si and ^{23}Na.[43–45]

In this work, we use a recently trained reactive MLIP at the dispersion-corrected *meta*-GGA level of DFT, designed for applications in water-loaded aluminosilicate zeolites,[37] to explore the aluminium distributions in industrially important zeolite RTH.[47,48] Simulations of a nanosecond duration, from which properly thermalized, averaged structures are extracted, allow us to extend far beyond the limitations of density functional theory calculations, without significant loss of accuracy. A KRR model was trained to obtain chemical shifts, allowing for direct predictions of NMR spectra, the assignment of peaks, and the analysis of Al distribution. In doing so, we demonstrate the power of a combined experimental-theoretical approach to accurately characterise complex zeolites.

2. Experimental methods

Pure silica RTH zeolite was synthesized according to the procedure described in our previous work[30] using triisopropyl(methyl)phosphonium hydroxide as an organic structure directing agent (OSDA). The sample, containing an F/OSDA = 1 molar ratio, was submitted to a thermal treatment in the presence of H_2 (60% v/v in N_2) at 750 °C for 2 h to remove the P counterpart of the OSDA. After that, the darkish sample was submitted to a calcination under O_2 at 700 °C for 4 h to remove the carbonaceous part. The resulting sample is labelled as RTH-SiO_2.

The Al-containing RTH zeolites were prepared according to the following synthesis gel composition: $1SiO_2 : xAl_2O_3 : 0.4\ OSDA^+OH^- : 10H_2O : 0.4HF$, x = 0.016 and 0.008, obtaining RTH_{16} (Si/Al = 16) and RTH_{28} (Si/Al = 28) zeolites, respectively. The OSDA employed for the Al-containing zeolites was diethyl diisopropyl ammonium (EPA), which was synthesized by the reaction of ethyl iodide (99 wt%, Alfa-Aesar) and

Open Access Article. Published on 28 January 2026. Downloaded on 6/13/2026 11:29:15 AM. This article is licensed under a Creative Commons Attribution-NonCommercial 3.0 Unported Licence.

ethyldiisopropylamine (99 wt%, Alfa-Aesar). The synthesis gel was placed into stainless steel autoclaves for 14 days at 175 °C. After that, the two samples were calcined at 550 °C for 2 h.

X-ray diffraction patterns were obtained by using a CUBIX (PANalytical) instrument operating at 45 kV and 40 mA (Kα of Cu (λ_1 = 1.5406 Å, λ_2 = 1.5444 Å, I_2/I_1 = 0.5)). The chemical composition of the zeolites was determined by inductively coupled plasma optical emission spectroscopy in a Varian 710-ES instrument.

^{27}Al and ^{29}Si solid-state NMR experiments were performed at 9.4 T using a Bruker Avance III HD spectrometer, at Larmor frequencies of 104.26 MHz and 79.45 MHz for ^{27}Al and ^{29}Si, respectively. One-dimensional (1D) quantitative ^{29}Si MAS NMR spectra were recorded with a 7 mm probehead spinning the sample at 5 kHz, with a 60° flip angle pulse of 4 μs, corresponding to a radio frequency (RF) field of *ca.* 41 kHz). The ^{29}Si–^{29}Si double quantum-single quantum (DQ-SQ) MAS NMR spectrum was acquired by applying a $SR26_{11}^{4}$-type sequence with recoupling times of 4, 6 and 8 ms. Two-dimensional (2D) dipolar-mediated heteronuclear multiple-quantum coherence D-HMQC ^{29}Si–^{27}Al NMR spectra were obtained with a 4 mm triple resonance MAS Bruker probehead with the sample spinning at 10 kHz. The pulse durations corresponded to RF fields of 8 kHz and 20 kHz for ^{27}Al and ^{29}Si, respectively. Dipolar recoupling ($SR4_1^2$ sequence) of 1.8, 1.2 and 0.6 ms and a recycling delay of 0.5 s were applied.

^{27}Al and ^{29}Si NMR spectra performed at 17.6 T were acquired using a Bruker Avance Neo spectrometer with Larmor Frequencies of 195.44 MHz and 148.99 MHz for ^{27}Al and ^{29}Si, respectively. 1D quantitative ^{27}Al MAS and 2D ^{27}Al MQMAS NMR spectra were obtained with a 2.5 mm double resonance MAS Bruker probehead at a spinning rate of 30 kHz. The 2D MQMAS spectra were acquired with excitation and reconversion pulse durations of 4 μs and 1.5 μs (RF field of *ca.* 107 kHz), respectively, a central-transition selective pulse of 11 μs (field of *ca.* 10 kHz) for detection, and 32 t_1-increments (experimental time of 100 min). The 2D ^{29}Si–^{27}Al D-HMQC NMR spectra were obtained with a 4 mm triple resonance MAS Bruker probehead with a rotor sample spinning frequency of 10 kHz. RF fields of 6 kHz and 20 kHz were used for ^{27}Al and ^{29}Si, respectively, and a dipolar recoupling ($SR4_1$ sequence) of 1.8 ms was applied on the ^{29}Si channel. 24 t_1-increments and a recycling delay of 0.2 s were used (experimental time of 53 h). For details of the KRR training, computational determination of chemical shifts, error analysis and model validation, see SI Sections S1–4, S7 and S9.

3. Results and discussion

A 1D ^{29}Si MAS-NMR spectrum of the pure silica RTH zeolite has been reported before,[49] but not with high resolution. Here, RTH was synthesized in pure silica form, in addition to aluminosilicate forms with Si : Al atomic ratios of 16 and 28. We observe four signals of equal intensity in the ^{29}Si MAS NMR spectrum of the RTH-SiO_2 zeolite (Fig. 1a), corresponding to Si Q^4(0Al) environments, labelled from left to right as A–D. This observation aligns with the RTH topology, which contains four crystallographic Si sites of equal multiplicity. According to the F/

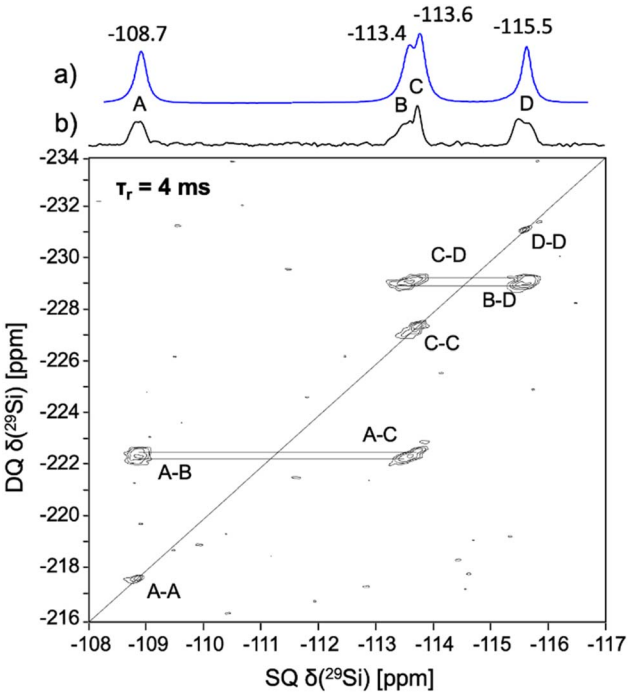

Fig. 1 (a) 1D ^{29}Si MAS NMR spectrum and (b) 2D ^{29}Si–^{29}Si DQ-SQ MAS NMR spectrum at recoupling time of 4 ms for the sample RTH-SiO_2.

OSDA = 1 molar ratio in the sample, the OSDA cations are charge balanced by fluoride, ruling out the presence of connectivity defects in the structure, as further supported by the absence of any signal at around $\delta(^{29}Si) \approx -104$ ppm, which is characteristic of Q^3 sites.[30]

In order to assign the ^{29}Si NMR peaks of the RTH-SiO_2 zeolite to specific crystallographic sites, we recorded the dipolar-based 2D double quantum-single quantum (DQ-SQ) ^{29}Si spectrum (Fig. 1b). In this spectrum, the indirect dimension of the cross-peaks reflects the sum of the chemical shifts of dipolar-coupled ^{29}Si sites, providing insights into their connectivity. By comparing these connectivity patterns with structural information on the RTH topology available in the IZA database,[50] we were able to assign the ^{29}Si signals to individual crystallographic T-sites within the framework (Table 1). This allows the assignment of signal B to T_3 site based on the observation that it is the only silicon position connected to only two other sites (T_1 and T_4). Signal C was assigned to T_2 since it is missing a cross-peak with signal B (T_3). Theoretical calculations are necessary for the assignment of signals A and D.

Table 1 Connectivity matrix for T-sites in RTH extracted from the IZA database[50] and ^{29}Si DQ-SQ cross-peaks from Fig. 1b

IZA matrix					NMR matrix				
	T_1	T_2	T_3	T_4		A	B	C	D
T_1	1	1	2	0	A	X	X	X	—
T_2	1	2	0	1	B	X	—	—	X
T_3	2	0	0	2	C	X	—	X	X
T_4	0	1	2	1	D	—	X	X	X

 This journal is © The Royal Society of Chemistry 2026

Open Access Article. Published on 28 January 2026. Downloaded on 6/13/2026 11:29:15 AM. This article is licensed under a Creative Commons Attribution-NonCommercial 3.0 Unported Licence.

For the computational prediction of ^{29}Si chemical shifts of T_1–T_4 sites in RTH-SiO_2, a purely siliceous model of RTH was used,[50] with no intercalated water molecules, in order to match the conditions within the hydrophobic RTH-SiO_2 pore. The calculated ^{29}Si chemical shifts, collected in Table 2, spread over a range of 8 ppm. Comparison with the ^{29}Si MAS NMR spectrum in Fig. 1a allows assignment of the peak D to the T_1 ($\delta(^{29}$Si-KRR) = −116.2 ppm), and the peak A to T_4 ($\delta(^{29}$Si-KRR) = −108.3 ppm). The calculated ^{29}Si chemical shifts of T_2 and T_3 sites are separated by only 0.3 ppm, with T_2 having slightly higher chemical shift. However, this minor difference falls within the KRR model's margin of error (Table S1).

Overall, the average deviation of the theoretical predictions from experiment is only 0.4 ppm, aligning with the expected error of the KRR model.

Having assigned the ^{29}Si NMR peaks for RTH-SiO_2, we next investigated the siting of aluminium in the framework of Al-RTH, using zeolites prepared at two Si/Al atomic ratios: RTH_{16} (Si/Al = 16) and RTH_{28} (Si/Al = 28). The ^{27}Al MAS NMR spectra of both zeolites show a very intense signal at $\delta(^{27}$Al-exp) = 56.8 ppm, and another weaker at $\delta(^{27}$Al-exp) = 60.8 ppm. Quantification of the peak areas suggests that the peak at 60.8 ppm accounts for about 15% of total aluminium (Fig. 2a), and thus, assuming the peak corresponds to a single T-site, there is a slight underpopulation of that T-site, compared with 25% expected under the assumption of a random distribution of aluminium among the four T-sites.

While the ^{29}Si chemical shift can be directly obtained from the position of the peak maximum, the isotropic chemical shift of ^{27}Al requires special consideration due to its quadrupolar nature. In particular, strong quadrupolar interactions can cause ^{27}Al resonances to become broad and asymmetric, with the peak maximum shifted to lower chemical shift values than the actual isotropic shift.[51] The 2D MQ-MAS ^{27}Al NMR spectrum (Fig. S6) with the two signals along the diagonal indicate that the aluminium atoms are in a non-distorted tetrahedral environment. To accurately extract these shifts, we simulated the 2D MQMAS ^{27}Al NMR spectrum assuming that the intense high-field signal arises from three distinct aluminium sites. This simulation enabled the assignment of the isotropic ^{27}Al chemical shifts corresponding to the four crystallographic T-sites, as summarized in Table 2.

To assign the ^{27}Al NMR peaks to specific crystallographic T-sites of the RTH structure, computational predictions of ^{27}Al chemical shifts were performed using a high-silica RTH model with a Si/Al ratio of 31 (RTH_{31}). In this model, Al pairing is minimized, with Al–Al distances exceeding 10 Å. This was also confirmed by creating models with a Si/Al ratio of 63, which showed only a minor effect on the resulting chemical shifts (see Section S8 in the SI for details). The calculations used defect-free RTH structures containing one aluminium atom per unit cell and five water molecules, closely reproducing the experimental conditions (Si/Al = 28, water concentration = 4 wt% revealed by thermogravimetric analysis, corresponding to 4.5 water molecules per unit cell). However, different water loadings were tested, and it was shown that the precise water content has minimal effect on the ^{27}Al NMR chemical shift (see Section S7 in the SI).

The computed ^{27}Al NMR shifts, shown in Table 2, fall into two classes, one centered in the range between 57.4 ppm and 59.9 ppm, comprising the peaks for T_1, T_2 and T_3, and one at a higher shift (61.8 ppm), for the underpopulated T_4 site, confirming that the higher shift peak belongs to a single T-site. The spread of the ^{27}Al shifts is 4.4 ppm (Table 2). The ^{29}Si NMR spectra of samples RTH_{16} and RTH_{28} are broader than that of the RTH-SiO_2, as displayed in Fig. 2b, because of the new Si–O–Al environments and especially the quadrupolar character of the ^{27}Al nuclei. Indeed, the spectrum of the RTH_{28} sample with lower aluminium content shows a better resolution with three main ^{29}Si signals at −108.8, −113.7, and −115.9 ppm.

The effect of neighbouring aluminium atoms on the ^{29}Si NMR chemical shifts was also predicted by KRR, *via* calculation of all ^{29}Si shifts in the RTH_{31} model. Table 2 shows the ^{29}Si chemical shifts of all Si atoms that are nearest neighbours to an aluminium placed at a specific T-site. These ^{29}Si chemical shifts are higher by 7 ppm on average than in the pure silica structure. This shift is not entirely uniform and the chemical shifts have to be calculated explicitly. However, some general trends can be obtained, such as T_4 always having the highest ^{29}Si chemical shift.

It is clear from Table 2 that there is close agreement between the calculated and experimentally observed ^{27}Al and ^{29}Si NMR chemical shifts, and that KRR predicts the expected 1 : 2 : 1 and 1 : 3 patterns that are observed in ^{29}Si and ^{27}Al NMR spectra, respectively. Thus, we find that the MLIP-KRR method is able to accurately predict the experimental chemical shift for both aluminium and silicon atoms in RTH, and assign the peaks in the spectra, reducing the requirement for expensive *operando* modelling at the DFT level.[35,43] The significance of considering dynamical averages over long trajectories for the prediction of shifts is clear from Section S2/Table S1, in which it is observed

Table 2 Calculated and experimental ^{27}Al and ^{29}Si NMR chemical shifts (ppm) for both RTH-SiO_2 and Al-RTH. The ^{29}Si chemical shifts of silicon atoms neighbouring the aluminium atoms were calculated using the Al-RTH_{31} model

	RTH-SiO_2		RTH_{31}		
T site	$\delta(^{29}$Si-KRR)	$\delta(^{29}$Si-exp)	$\delta(^{27}$Al-KRR)	$\delta(^{27}$Al-exp)	$\delta(^{29}$Si-KRR)
T_1	−116.2	−115.5	59.9	58.1	−107.0 (T_1)
					−104.7 (T_3)
					−107.1 (T_2)
					−105.5 (T_3)
T_2	−113.4	−113.6	58.6	57.2	−102.0 (T_4)
					−106.3 (T_1)
					−108.4 (T_2)
					−105.2 (T_2)
T_3	−113.7	−113.4	57.4	56.6	−106.1 (T_1)
					−106.4 (T_1)
					−101.1 (T_4)
					−102.9 (T_4)
T_4	−108.3	−108.7	61.8	61.2	−105.6 (T_3)
					−101.9 (T_4)
					−106.4 (T_3)
					−105.8 (T_2)

Open Access Article. Published on 28 January 2026. Downloaded on 6/13/2026 11:29:15 AM.
This article is licensed under a Creative Commons Attribution-NonCommercial 3.0 Unported Licence.

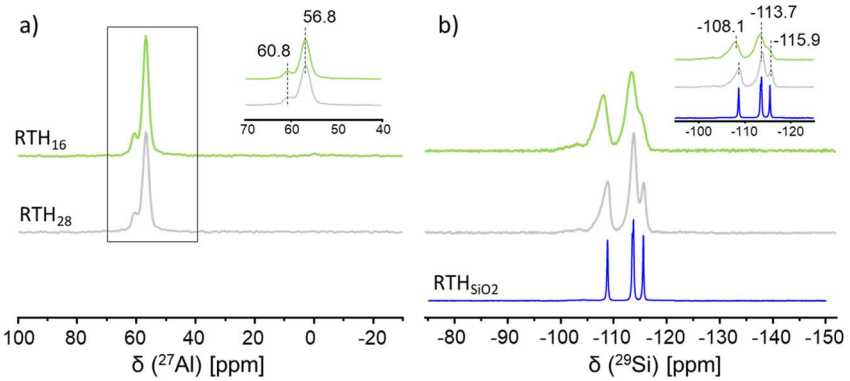

Fig. 2 (a) ^{27}Al MAS-NMR spectra measured at 750 MHz spectrometer for samples with Si/Al ratio of 16 and 28. (b) ^{29}Si MAS-NMR spectra measured at 400 MHz spectrometer of the same RTH and the RTH-SiO_2 samples.

that the chemical shift varies over around 10 ppm along the trajectory, and single structure DFT predictions may give entirely the wrong assignment of T sites. By contrast, provided long-term averages were considered, any reasonable fit was successful, including the bond angle correlation of Lipmaa, or the two parameter "angle plus bond length" fit derived from LASSO regression.

Having assigned the spectra, we next consider the siting of Al among the four T sites. The quantitative 1D ^{27}Al NMR spectrum of the RTH_{28} sample in Fig. 2 shows that the resonance at 60.8 ppm, assigned to Al in the T_4 site, accounts for approximately 15%, while the more intense signal at 56.8 ppm, attributed to Al in the T_1–T_3 sites, represents the remaining 85%. The 750 MHz ^{27}Al MQMAS NMR spectrum (Fig. S7) showed that a distribution of chemical shifts were present in the lower shift peak, which, when fitted according to an assumed Czjzek distribution, indicated three signals are likely to be present (see Section S5), corresponding to T_1, T_2 and T_3. However, the limited resolution of this signal prevents reliable quantification of the individual aluminium contributions at these three sites.

In order to identify the occupation of those three T sites, we employ recoupling methods, which provide information about through-space interatomic distances. While such methods are widely used for spin-1/2 nuclei, typically through cross-polarization (CP),[33] it remains challenging to achieve efficient spin-locking of the central transition of quadrupolar nuclei,[52] such as ^{27}Al. Several methods have been developed to overcome this limitation, among which D-HMQC NMR experiments have been introduced and successfully used to recouple spin 1/2 nuclei with quadrupolar nuclei.[53,54] For example, for zeolites, the $SR4_1^2$ sequence based on supercycled symmetry has been used.[55] Herein, we measured the D-HMQC spectrum of the RTH_{28} sample, which was selected because of its lower Al content, which simplifies the Al–Si correlations and thus interpretation of the data (Fig. 3).

In order to interpret the experimental spectrum and assign peaks to crystallographic sites, it is valuable to calculate the correlation peaks *via* quantum chemical methods, such as DFT. Recently, an attempt to determine the aluminium siting in zeolite ZSM-5 using the ^{29}Si–^{27}Al D-HMQC NMR experiments in tandem with static DFT calculations was undertaken by Dib *et al.*[22] Nevertheless, we have recently observed that the role of water loading and framework dynamics is significant in the assignment of chemical shifts to T sites in complex zeolites, even under mild conditions, such as room temperature and atmospheric humidity.[36] Hence, in the current work, we utilize the speed and accuracy of our MLIP-KRR approach to obtain dynamically averaged chemical shifts for all correlations, accounting for nearest and next-nearest neighbours. The predicted peaks are superimposed on the experimental spectrum, showing close agreement between theory and experiment.

Modelling shows that for the nearest neighbour (NN) sites, which are expected to be the strongest signals, there is a clustering between 61 and 54 ppm along the Al axis and between −101 and −108 ppm in the indirect (^{29}Si) dimension. However,

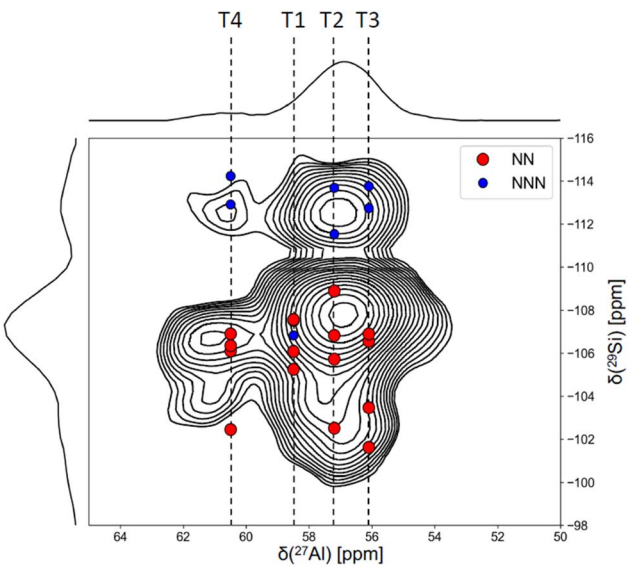

Fig. 3 ^{29}Si–^{27}Al D-HMQC MAS NMR spectrum of the sample RTH_{28} with a recoupling time of 1.8 ms recorded at 750 MHz. The data extracted from the theoretical calculations is superimposed. Chemical shifts have been adjusted by a constant factor to match the peaks and to correct for any minor systematic inaccuracies in transforming the shielding into chemical shift (see S3 in SI for more details).

 This journal is © The Royal Society of Chemistry 2026

Open Access Article. Published on 28 January 2026. Downloaded on 6/13/2026 11:29:15 AM.
This article is licensed under a Creative Commons Attribution-NonCommercial 3.0 Unported Licence.

the experimental spectrum in Fig. 3 also shows a cross-peak centered around (57, −113) ppm, which cannot be explained by nearest neighbour pairs. These cross-peaks are predicted by the KRR model to be due to the next nearest neighbour (NNN) contributions in this region of the spectrum, which are derived from short distance, throughspace interactions in the 4-ring of RTH, and thus may be expected to contribute to the experimental spectrum. Other NNN sites are too distant to contribute signficantly to the spectrum, and are thus neglected.

To test this hypothesis, we performed numerical simulations using the SIMPSON code,[56] which revealed that the magnetization transfer from a ^{27}Al nucleus to its four NN ^{29}Si atoms, at an average distance of 3.5 Å, occurs much faster than to the NNN ^{29}Si at 4.5 Å (Fig. 4), (see Section S6 in SI for more details). This finding implies that the contribution of close NNN peaks to the spectrum will vary with mixing time.

The prediction was validated by recording three ^{29}Si–^{27}Al D-HMQC NMR spectra using mixing times of 600 μs, 1200 μs, and 1800 μs under similar conditions to those used in the SIMPSON simulations. The spectra displayed in Fig. 4, show that at the shortest mixing time (600 μs), the crosspeak corresponding to NN pairs centered at (57, −109) ppm is visible, while the cross-peak at (57, −113) ppm, associated with the NNN site, is not detectable. At longer mixing times, 1200 and 1800 μs, the cross-peak from NNN site becomes progressively more pronounced, confirming successful polarization transfer to the more distant T-site. This observation supports the KRR-based prediction hypothesis that the (57, −113) ppm cross-peak arises from NNN interactions across the 4-ring.

Upon full characterisation of the D-HMQC NMR spectrum, and assignment of all relevant NN and NNN peaks, we are in a position to approximately quantify the spectrum, and thus the Al siting among the four T sites. Detailed inspection of the 2D ^{29}Si–^{27}Al D-HMQC NMR spectrum reveals that both ^{27}Al signals centred at about 61 and 57 ppm exhibit correlation to three distinct ^{29}Si components in the indirect dimension. Simulation of the ^{29}Si projections at each ^{27}Al position enables quantification of these contributions (Fig. S14). To get quantitative results, we need to simulate the magnetization transfer due to the non-quantitative nature of the D-HMQC experiment, where cross-peaks from NNN Si atoms are weaker than those from NN cross-peaks (Fig. S10).

Magnetization transfer between ^{29}Si–^{27}Al pairs was calculated with the SIMPSON code using the same sequence and experimental parameters used to record experimental D-HMQC NMR spectrum. For NNN Si sites, the resulting signals correspond to roughly 35% of the intensity observed for NN Si sites. The combined analysis of the projections, and peak compositions predicted by the KRR method (Fig. 3) allows for quantifying the contributions of all T-sites. Decomposing the D-HMQC NMR spectrum into five distinct peaks and combining the intensity information with the predicted peak compositions allows the construction of a system of linear equations:

$$0\cdot t_1 + 0\cdot t_2 + 0\cdot t_3 + (4T_4^{NN} + 2T_4^{NNN})\cdot t_4 = 14,$$

$$0\cdot t_1 + (2T_2^{NNN})\cdot t_2 + (2T_3^{NNN})\cdot t_3 + 0\cdot t_4 = 12,$$

$$(4T_1^{NN} + 1\cdot T_1^{NNN})\cdot t_1 + (3T_2^{NN})\cdot t_2 + (2T_3^{NN})\cdot t_3 + 0\cdot t_4 = 58,$$

$$0\cdot t_1 + (1T_2^{NN})\cdot t_2 + (2T_3^{NN})\cdot t_3 + 0\cdot t_4 = 16.$$

In this system, the variables t_i correspond to the normalized populations of aluminium at each T-site, while the coefficients T_i^{NN} and T_i^{NNN} represent the relative contributions of nearest-neighbor (NN) and next-nearest-neighbor (NNN) silicon sites to the D-HMQC NMR signal for each T-site. Solving the system yields an approximate quantitative distribution of aluminium across the four crystallographic T-sites in the RTH framework, with the following T-site occupations:

$$t_1 = 15 \pm 12\% \quad (1)$$

$$t_2 = 64 \pm 23\% \quad (2)$$

$$t_3 = 8 \pm 12\% \quad (3)$$

$$t_4 = 14 \pm 0.2\% \quad (4)$$

The uncertainties in t_i were estimated by varying each T_i parameter within its error range (Fig. 5). The higher the

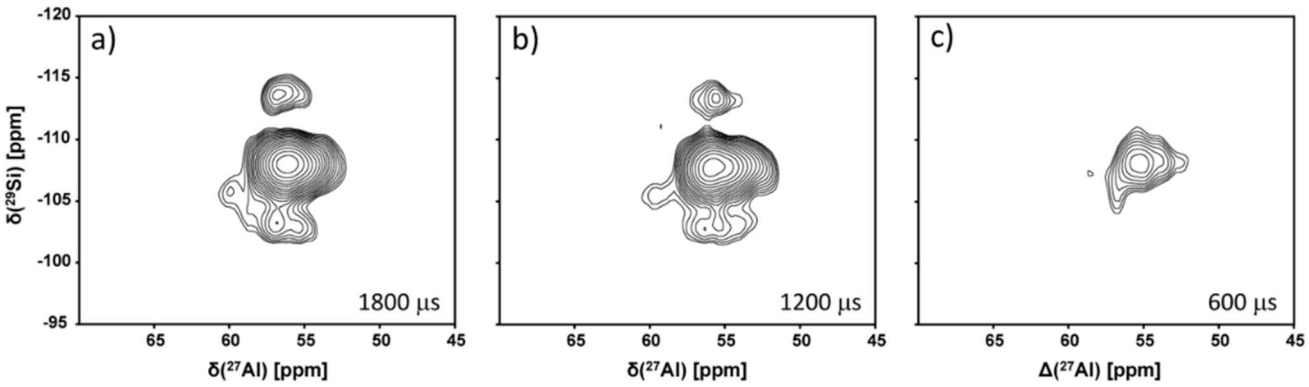

Fig. 4 ^{29}Si–^{27}Al D-HMQC MAS-NMR spectra of the sample RTH$_{28}$ measured at 400 MHz with recoupling time of (a) 1800 μs, (b) 1200 μs, and (c) 600 μs.

Open Access Article. Published on 28 January 2026. Downloaded on 6/13/2026 11:29:15 AM.
This article is licensed under a Creative Commons Attribution-NonCommercial 3.0 Unported Licence.

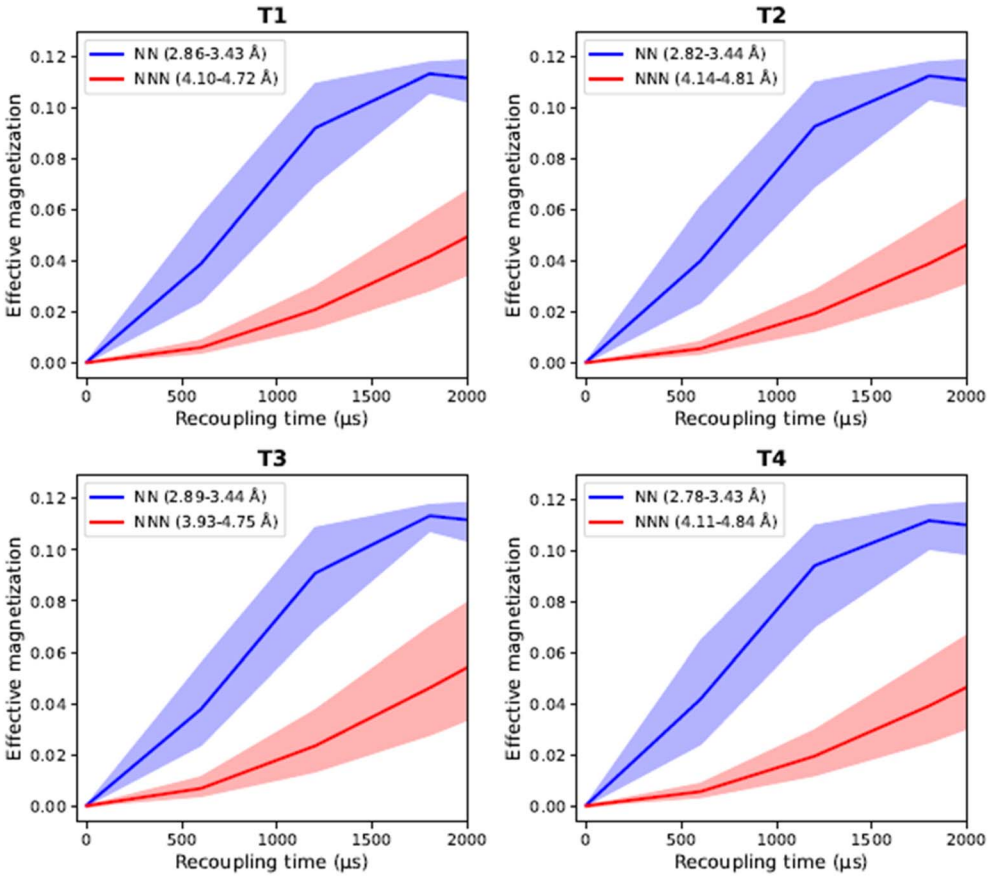

Fig. 5 Magnetization transfer simulations were performed for each T-site in zeolite RTH as a function of recoupling time in the NMR experiment. The shaded area indicates the standard deviation over different Si–Al distances sampled in the MD simulation. Further details are provided in SI Section S6.

variation of bond lengths during the dynamical simulation, the wider the range, and the larger the uncertainty in the prediction of effective magnetization, for a given T site. This in turn affects the errors in the final prediction of occupancies. Furthermore, the more highly coupled one T site is to the others, the higher the error in prediction, due to error propagation. This gives rise to higher errors for T_2 than T_1/T_3. Conversely, T_4, which is totally decoupled from the other sites, has the lowest error. The low error for the T_4 site arises from its isolated peak in the 2D spectra, resulting in a correspondingly low uncertainty.

The analysis indicates that the T_2 site is the most populated, despite the relatively large uncertainty ($t_2 = 64 \pm 23\%$), while the T_1, T_3, and T_4 sites have significantly lower populations. Notably, the T_4 site occupancy ($t_4 = 14 \pm 0.2\%$) closely reproduces the value obtained from the quantitative 1D spectrum (Fig. 2a), with the small uncertainty (1%) likely reflecting the peak fitting in the experimental data. The T_2 site is the most accessible in RTH, as it is the only site that connects the dense layers together, which are made up of T_1, T_3 and T_4. T_2 lies in accessible 4 rings, surrounded by void space in two directions. Conversely, the T_3 site is the least accessible, lying deeper in the dense region of the framework than all other sites. These accessibilities are consistent with the predicted occupations.

This methodology establishes a solid foundation for future studies on the prediction of Al siting in complex zeolites under *operando* conditions. Future work will employ full NMR spectra and EFG tensors, going beyond the limits of chemical shifts and enabling more accurate and detailed quantitative predictions.

4. Conclusions

In this study, we successfully assigned the NMR spectra of siliceous and Al-containing zeolite RTH for the first time, using a combination of experimental multinuclear NMR techniques and a computational framework based on neural network potentials and kernel ridge regression. The excellent agreement between the predicted spectra from the theoretical calculations and experimental results highlights the accuracy and predictive capabilities of this machine learning approach, which goes far beyond the capacities of traditional electronic structure calculation methods, in terms of both model realism and probing ^{29}Si–^{27}Al connectivity in zeolites, from which deeper insight into the aluminium siting and framework connectivity can be obtained, including approximate quantification of Al location.

Conflicts of interest

The authors have no conflicts of interest to declare.

This journal is © The Royal Society of Chemistry 2026

Open Access Article. Published on 28 January 2026. Downloaded on 6/13/2026 11:29:15 AM. This article is licensed under a Creative Commons Attribution-NonCommercial 3.0 Unported Licence.

Data availability

The RTH structures, KRR models, training databases for ^{27}Al and ^{29}Si chemical shifts are available at DOI: https://doi.org/10.5281/zenodo.16318441.

Supplementary information (SI): information on the structures, KRR training, and molecular dynamics simulations can be found in the SI, along with a detailed analysis of the experimental data. See DOI: https://doi.org/10.1039/d5ta09253a.

Acknowledgements

Charles University Centre of Advanced Materials (CUCAM) (OP VVV Excellent Research Teams, project number CZ.02.1.01/0.0/0.0/15003/0000417) is acknowledged. This work was supported by the Ministry of Education, Youth and Sports of the Czech Republic through the e-INFRA CZ (ID: 90254). CJH acknowledges support *via* the ERC_CZ project LL 2104. CJH, AE, DBA and LG acknowledge the Czech Science Foundation (CJH: GAČR standard project 23-07616S). CB acknowledges the funding from the European Union's Horizon Europe research and innovation program under the ERA-PF grant agreement no. 101180584. This work was supported by MICIU/AEI/10.13039/501100011033 (projects CEX2021–001230-S), co-funded by the ERDF/EU (PID2022–136934OB-I00) and by the European Union NextGeneration EU/PRTR (TED2021–130191B-C41). Grant CIPROM/2024/050 funded by Generalitat Valenciana is acknowledged. PANACEA project funded by the European Union's Horizon 2020 research and innovation program under grant agreement no. 101008500 is acknowledged.

References

1 S. Al-Nahari, E. Dib, C. Cammarano, E. Saint-Germes, D. Massiot, V. Sarou-Kanian and B. Alonso, *Angew. Chem., Int. Ed.*, 2023, **62**, e202217992.
2 J. Dědeček, E. Tabor and S. Sklenak, *ChemSusChem*, 2019, **12**, 556–576.
3 L. Zhao, P.-P. Xiao, Y. Wang, Y. Lu, T. M. Karim, H. Gies and T. Yokoi, *ACS Appl. Mater. Interfaces*, 2024, **16**, 17701–17714.
4 S. Wang, P. Wang, Z. Qin, Y. Chen, M. Dong, J. Li, K. Zhang, P. Liu, J. Wang and W. Fan, *ACS Catal.*, 2018, **8**, 5485–5505.
5 C. Deng, J. Zhang, L. Dong, M. Huang, B. Li, G. Jin, J. Gao, F. Zhang, M. Fan, L. Zhang and Y. Gong, *Sci. Rep.*, 2016, **6**, 23382.
6 Z. Ma, D. Shi, S. Wang, M. Dong and W. Fan, *Front. Chem. Sci. Eng.*, 2024, **18**, 86.
7 P. Xiao, X. Tang, H. Toyoda, Y. Wang, A. Zheng, L. Wang, J. Huang, M. Sawada, K. Nakamura, Y. Wang, H. Gies and T. Yokoi, *Angew. Chem., Int. Ed.*, 2025, **64**, e202506023.
8 T. Liang, J. Chen, Z. Qin, J. Li, P. Wang, S. Wang, G. Wang, M. Dong, W. Fan and J. Wang, *ACS Catal.*, 2016, **6**, 7311–7325.
9 K. Fan, S. Liu, Y. Ma, Q. Wu, S. Wang, A. Pauschinger, A.-N. Parvulescu, N. Bottke, T. Yokoi, D. E. De Vos, X. Meng, W. Zhang and F.-S. Xiao, *Ind. Eng. Chem. Res.*, 2025, **64**, 9650–9655.
10 A. T. Smith, P. N. Plessow and F. Studt, *J. Phys. Chem. C*, 2021, **125**, 20373–20379.
11 E. Tabor, M. Bernauer, B. Wichterlová and J. Dedecek, *Catal. Sci. Technol.*, 2019, **9**, 4262–4275.
12 J. Li, M. Gao, W. Yan and J. Yu, *Chem. Sci.*, 2023, **14**, 1935–1959.
13 J. Bae and M. Dusselier, *Chem. Commun.*, 2023, **59**, 852–867.
14 A. B. Pinar, L. Gómez-Hortigüela, L. B. McCusker and J. Pérez-Pariente, *Chem. Mater.*, 2013, **25**, 3654–3661.
15 J. R. Di Iorio and R. Gounder, *Chem. Mater.*, 2016, **28**, 2236–2247.
16 Z. Xiong, G. Qi, L. Bai, E. Zhan, Y. Chu, J. Xu, N. Ta, A. Hao, F. Deng and W. Shen, *Catal. Sci. Technol.*, 2022, **12**, 4993–4997.
17 B. C. Knott, C. T. Nimlos, D. J. Robichaud, M. R. Nimlos, S. Kim and R. Gounder, *ACS Catal.*, 2018, **8**, 770–784.
18 C. Bornes, M. Fischer, J. A. Amelse, C. F. G. C. Geraldes, J. Rocha and L. Mafra, *J. Am. Chem. Soc.*, 2021, **143**, 13616–13623.
19 A. B. Pinar, P. Rzepka, A. J. Knorpp, L. B. McCusker, C. Baerlocher, T. Huthwelker and J. A. Van Bokhoven, *J. Am. Chem. Soc.*, 2021, **143**, 17926–17930.
20 G. Li, C. Foo, R. Fan, M. Zheng, Q. Wang, Y. Chu, J. Li, S. Day, P. Steadman, C. Tang, T. W. B. Lo, F. Deng and S. C. E. Tsang, *Science*, 2025, **387**, 388–393.
21 P. Rzepka, T. Huthwelker, J. Dedecek, E. Tabor, M. Bernauer, S. Sklenak, K. Mlekodaj and J. A. Van Bokhoven, *Science*, 2025, **388**, 423–428.
22 E. Dib, T. Mineva, E. Veron, V. Sarou-Kanian, F. Fayon and B. Alonso, *J. Phys. Chem. Lett.*, 2018, **9**, 19–24.
23 S. Sklenak, J. Dědeček, C. Li, B. Wichterlová, V. Gábová, M. Sierka and J. Sauer, *Phys. Chem. Chem. Phys.*, 2009, **11**, 1237–1247.
24 J. Holzinger, P. Beato, L. F. Lundegaard and J. Skibsted, *J. Phys. Chem. C*, 2018, **122**, 15595–15613.
25 J. Holzinger, M. Nielsen, P. Beato, R. Y. Brogaard, C. Buono, M. Dyballa, H. Falsig, J. Skibsted and S. Svelle, *J. Phys. Chem. C*, 2019, **123**, 7831–7844.
26 J. Martinez-Ortigosa, R. Millán, J. Simancas, J. A. Vidal-Moya, C. Martineau-Corcos, F. Rey and T. Blasco, *Inorg. Chem. Front.*, 2025, **12**, 2359–2367.
27 J. Martinez-Ortigosa, J. Simancas, J. A. Vidal-Moya, F. Rey, S. Valencia and T. Blasco, *Appl. Sci.*, 2021, **11**, 6850.
28 T. Blasco, A. Corma, M. J. Díaz-Cabañas, F. Rey, J. A. Vidal-Moya and C. M. Zicovich-Wilson, *J. Phys. Chem. B*, 2002, **106**, 2634–2642.
29 D. H. Brouwer, C. C. Brouwer, S. Mesa, C. A. Semelhago, E. E. Steckley, M. P. Y. Sun, J. G. Mikolajewski and C. Baerlocher, *Microporous Mesoporous Mater.*, 2020, **297**, 110000.
30 J. Martinez-Ortigosa, R. Millán, J. Simancas, M. Hernández-Rodríguez, J. A. Vidal-Moya, J. L. Jordá, C. Martineau-Corcos, V. Sarou-Kanian, M. Boronat, T. Blasco and F. Rey, *J. Mater. Chem. A*, 2024, **12**, 876–891.
31 Z. J. Berkson, M. Hsieh, S. Smeets, D. Gajan, A. Lund, A. Lesage, D. Xie, S. I. Zones, L. B. McCusker, C. Baerlocher and B. F. Chmelka, *Angew. Chem., Int. Ed.*, 2019, **58**, 6255–6259.

Open Access Article. Published on 28 January 2026. Downloaded on 6/13/2026 11:29:15 AM.
This article is licensed under a Creative Commons Attribution-NonCommercial 3.0 Unported Licence.

32 K. Chen, S. Horstmeier, Vy. T. Nguyen, B. Wang, S. P. Crossley, T. Pham, Z. Gan, I. Hung and J. L. White, *J. Am. Chem. Soc.*, 2020, **142**, 7514–7523.
33 C. A. Fyfe, K. C. Wong-Moon, Y. Huang, H. Grondey and K. T. Mueller, *J. Phys. Chem.*, 1995, **99**, 8707–8716.
34 G. J. Kennedy, J. W. Wiench and M. Pruski, *Solid State Nucl. Magn. Reson.*, 2008, **33**, 76–81.
35 C. Lei, A. Erlebach, F. Brivio, L. Grajciar, Z. Tošner, C. J. Heard and P. Nachtigall, *Chem. Sci.*, 2023, **14**, 9101–9113.
36 D. Willimetz, A. Erlebach, C. J. Heard and L. Grajciar, *Digit. Discov.*, 2025, **4**, 275–288.
37 A. Erlebach, M. Šípka, I. Saha, P. Nachtigall, C. J. Heard and L. Grajciar, *Nat. Commun.*, 2024, **15**, 4215.
38 V. Van Speybroeck, M. Bocus, P. Cnudde and L. Vanduyfhuys, *ACS Catal.*, 2023, **13**, 11455–11493.
39 T. G. Sours and A. R. Kulkarni, *J. Phys. Chem. C*, 2023, **127**, 1455–1463.
40 A. Erlebach, P. Nachtigall and L. Grajciar, *npj Comput. Mater.*, 2022, **8**, 174.
41 I. Saha, A. Erlebach, P. Nachtigall, C. J. Heard and L. Grajciar, *Catal. Sci. Technol.*, 2024, **14**, 5838–5853.
42 C. J. Heard, L. Grajciar and A. Erlebach, *Nanoscale*, 2024, **16**, 8108–8118.
43 C. Lei, C. Bornes, O. Bengtsson, A. Erlebach, B. Slater, L. Grajciar and C. J. Heard, *Faraday Discuss.*, 2025, **255**, 46–71.
44 C. Ben Mahmoud, L. A. M. Rosset, J. R. Yates and V. L. Deringer, *J. Chem. Phys.*, 2025, **163**, 024118.
45 Z. Chaker, M. Salanne, J.-M. Delaye and T. Charpentier, *Phys. Chem. Chem. Phys.*, 2019, **21**, 21709–21725.
46 A. F. Harper, T. Huss, S. S. Köcher and C. Scheurer, *Faraday Discuss.*, 2025, **255**, 411–428.
47 T. Yokoi, M. Yoshioka, H. Imai and T. Tatsumi, *Angew. Chem., Int. Ed.*, 2009, **48**, 9884–9887.
48 J. E. Schmidt, M. A. Deimund, D. Xie and M. E. Davis, *Chem. Mater.*, 2015, **27**, 3756–3762.
49 J. E. Schmidt, D. Xie and M. E. Davis, *Chem. Sci.*, 2015, **6**, 5955–5963.
50 C. Baerlocher, B. H. Darren, B. Marler and L. B. McCusker, Database of Zeolite Structures, https://www.iza-structure.org/databases/, accessed January 10, 2026.
51 B. Zibrowius and M. Felderhoff, *Phys. Chem. Chem. Phys.*, 2019, **21**, 12576–12584.
52 A. J. Vega, *J. Magn. Reson.*, 1992, **96**, 50–68.
53 Z. Gan, *J. Magn. Reson.*, 2007, **184**, 39–43.
54 J. Trebosc, B. Hu, J. P. Amoureux and Z. Gan, *J. Magn. Reson.*, 2007, **186**, 220–227.
55 A. Brinkmann and A. P. M. Kentgens, *J. Am. Chem. Soc.*, 2006, **128**, 14758–14759.
56 M. Bak, J. T. Rasmussen and N. C. Nielsen, *J. Magn. Reson.*, 2000, **147**, 296–330.

This journal is © The Royal Society of Chemistry 2026